Energy Management System based on S-shaped Functions for Series Hybrid Vehicle under a Fully Active Topology

Márcio Von Rondow Campos, Lucas Jonys Ribeiro Silva, Thales Augusto Fagundes, Rodolpho Vilela Alves Neves, Vilma Alves Oliveira, *Life Senior Member, IEEE* and Ricardo Quadros Machado, *Senior Member, IEEE*

***Abstract*—This paper proposes an energy management system (EMS) applied to a series hybrid vehicle (SHV) powered by an internal combustion engine (ICE) and a hybrid energy storage system (HESS) consisting of chemical batteries and supercapacitors. The EMS enables power sharing among the ICE and the HESS under a fully active topology to improve control flexibility, considering that the ICE-generator set and HESS efficiencies are limited to a specific power injection operating range and transient responses. In this context, power sharing is performed using S-shaped functions that focus on maximizing supercapacitor usability to reduce fuel consumption and battery current stress. The advantage of the S-shaped function lies on its easy configuration and reduced number of control parameters. Additionally, metaheuristic optimization is used to tune the S-shaped functions according to the sources requirements for optimal performance in standard driving cycles, while Lyapunov's indirect method performs the stability analysis of the control strategy. Finally, experimental and computational simulations are accomplished to evaluate the effectiveness of the proposed EMS compared with traditional methods and an optimal approach.**

***Index Terms*—Hybrid vehicle, energy management system, fully active topology, non-linear controller.**

NOMENCLATURE

Abbreviations

ac, dc	alternating and direct current
AUC	Artemis urban cycle
DP	dynamic programming
ECMS	equivalent consumption minimization strategy
EMS	energy management system
FLC	fuzzy logic controller
HESS	hybrid energy storage system
HV	hybrid vehicle
HWT	Haar Wavelet transform
ICE	internal combustion engine
LPF	low-pass filter
MPC	model predictive control
NEDC	New European drive cycle
NLF	non-linear function
NYC	New York bus cycle
OCT	Orange Country transit bus cycle
ODE	ordinary differential equations
PDL	Port Drawyage local cycle
PI	proportional integral
PMP	Pontryagin's minimum principle
PMSG	permanent magnetic synchronous generator
PWM	pulse width modulation
SHV	series hybrid vehicle
TIM	three-phase induction machine

Variables and constants

P_{load}, P_{max}	vehicle power and maximum load power
P_o	electrical component power losses
m, c, v_t	vehicle mass, drag coefficient and speed
V_{link}	dc-link voltage
V_{ref}, i_{ref}	dc-link voltage and current references
V_{min}, V_{max}	dc-link minimum and maximum voltage
i_{min}, i_{max}	dc-link minimum and maximum current
e_{link}	dc-link voltage error
e_{ps}	primary source current error
e_{sc}	supercapacitor current error
e_{bt}	battery current error
i_{Lps}, ips_{ref}	primary source current and its reference
i_{Lbt}, ibt_{ref}	battery current and its reference
i_{Lsc}, isc_{ref}	supercapacitor current and its reference
d_{ps}	primary source duty-cycle
d_{bt}	battery duty-cycle
d_{sc}	supercapacitor duty-cycle
d_{bk}	over-voltage protection duty-cycle
dbk_m	maximum over-voltage duty-cycle
P_{bk}	over-voltage protection dissipated power
V_{ps}, P_{ps}	primary source voltage and power
f_{rate}	fuel consumption
b_{ps}	constant fuel consumption rate
γ	unit conversion factor
ips_l, ips_u	primary source limit currents
Vsc_r	supercapacitor rated voltage

This work was supported by the Coordination for the Improvement of Higher Education Personnel (CAPES) under grants PDSE-88881.187771/2018-01, 88881.030370/2013-0 and 88887.682783/2022-00, the National Council for Scientific and Technological Development (CNPq) under grant 309624/2018-5, the Research Development Foundation (FUNDEP) Rota 2030/Line V under grant 27192/27 and the Sao Paulo Research Foundation (FAPESP) under grants 2020/05865-3, 2022/00628-9 and 2024/00607-7.

M. V. R. Campos, L. J. R. Silva, T. A. Fagundes, R. Q. Machado and V. A. Oliveira are with the Sao Carlos School of Engineering, University of Sao Paulo, Sao Carlos SP 13566-590, Brazil (e-mail: marciovonrondow@usp.br; lucasjonys@usp.br; thales.fagundes@usp.br; voliveira@usp.br; rquadros@sc.usp.br;).

R. V. A. Neves is with the Federal University of Viçosa, Viçosa MG 36570-900, Brazil (e-mail: rodolpho.neves@ufv.br).

Q_{bt}, V_{bt}, P_{bt}	battery capacity, voltage and power
SoC_{bt}	battery state-of-charge
SoC_m	battery minimum state-of-charge
SoC_{sc}	supercapacitor state-of-charge
ips_{nd}	non-filtered reference current
$i_{sc/bt}^{ref}$	HESS reference current
ibt_r	maximum battery recharge current
α_1, α_2, α_3	optimization tuning parameters
J	cost function
β_1, β_2, β_3	optimization weighting factors
t_{o_k}, t_{f_k}	driving cycle initial and final time
N_{dc}, $\boldsymbol{\psi}_{i,g}$	DE population size and mutant vector
μ_{de}, $\xi_{i,g}$	DE scaling factor and crossover
τ_{lpf}	LPF time constant
$\boldsymbol{x}$, $\boldsymbol{y}$	EMS model state vector and output vector
T_{tr}	traction machine torque
v_{tr}, v_{rs}	traction and resistance TIM velocity
j_a, j_d	inertia acceleration and deceleration

I. Introduction

THE increasing energy consumption and demand for vehicles in the recent years have raised concerns among environmentalists. The emission of polluting gases from non-renewable fuels for energy generation is taking the air quality and the environment to great risks. The transportation sector is a major contributor to the emissions of carbon monoxide, carbon dioxide, nitrogen oxides, and hydrocarbons, which are generated by burning fossil fuels [1]. This has drawn attention from countries around the world, who are taking action to reduce these emissions by proposing policies that promote the production of hybrid vehicles (HVs).

In this context, the HVs are the most feasible choices in the short-term for the automotive industry. The series hybrid vehicle (SHV) refers to vehicles driven by electric motors, with an internal combustion engine (ICE) used as the primary source and the batteries and/or the supercapacitors applied as auxiliary sources. In the SHV, the ICE used as primary source is coupled to the permanent magnetic synchronous generator (PMSG) with its power rectified and injected to the dc-link via dc/dc converters by allowing the energy storage devices to be charged [2], [3].

For these types of vehicles, the fully active topology consists of coupling multiple energy sources to the dc-link by using dc/dc converters. In the literature, the fully active topology is considered complex to be implement due to the high number of variables in the control strategy and reduced control stability. However, the dc/dc power converter is not only used to improve the multiple sources efficiency but also, to provide flexibility to the sources, operating according to their time responses and nominal requirements [4].

The ICEs show slower dynamic responses when compared to the batteries and supercapacitors, that is, they provide greater capacity of energy processing at steady-state regime [3]. On the other side, batteries have good energy capacity to compensate the transients, however they are more fragile when operate under extreme state-of-charge (SoC), which shorten their lifespan [5]. In the same way, supercapacitors have high cycles of recharging and can reach (supply or absorb) high levels of electrical power rapidly [6], but they have low autonomy in terms of power availability.

Therefore, considering the advantages and disadvantages of each energy source, an energy management system (EMS) is necessary for increasing the hybrid energy storage system (HESS) lifespan and save fuel of the primary source. To achieve the aforementioned targets, many optimization-based strategies have been developed in the literature [7]. In this context, the real-time optimization, as the equivalent consumption minimization strategy (ECMS) [8], [9] and model predictive control (MPC) [10], presents better performance under different drive cycles. Moreover, the learning-based strategies have been extensively used due to their superior performance [11], [12]. In [13], deep reinforcement learning is employed to improve fuel economy while maintaining a safe following distance between two vehicles. Additionally, in [12], a multi-agent reinforcement learning technique is applied to enhance fuel efficiency and reduce battery degradation, which was also utilized to optimize the ECMS in [14] and for velocity forecasting with MPC in [15].

Although optimal in performance, the computational effort of optimization-based strategies is higher, which limits their practical application [16]. Furthermore, learning-based methods also require large amounts of training data. These methods are more commonly explored in autonomous vehicles, where control actions are generated based on the interpretation of external environmental data, which still exhibit low reliability in terms of safety [17], [18]. In commercial HVs with multi-sources, due to computational effort and memory limitation, these strategies are not yet feasible for onboard computation units [19]. In order to resolve these practical limitations, EMS strategies based on rules were discussed in [4], [20], [21] employing deterministic, fuzzy or nonlinear controllers. The authors concluded that rule-based EMS are a good option for ensuring better communication speed, easy implementation and reliability in fully active topology for commercial HVs.

Nonlinear control strategies based on fuzzy logic controllers (FLCs) are widely used as EMS for vehicles supplied by multi-sources due to their practical implementation [22]. In this sense, the FLCs have shown to be robust in relation to parametric variations/uncertainties of the system, allowing adaptive adjustments to be made in real-time to fine-tune controller gains and enhance performance across different cycles to achieve the optimal result. The disadvantage of FLCs strategies is the high time consumed to tune the large number of parameters/rules, added by the complexity of building model-based closed-loop controllers and computational cost associated with defuzzification [23].

An adaptive fuzzy EMS was implemented in [24] to regulate the fuel cells power while it maintains the batteries SoC at a desired level for different circuits. However, this strategy was developed for a semi-active topology, where the batteries are directly coupled to the dc-link. Although this topology ensures stability, it lacks power-sharing flexibility and accelerates batteries degradation due to high voltage fluctuations in the dc-link under high power demands. Subsequently, this strategy

was enhanced in [21] by implementing an EMS using FLC based on frequency decoupling between fuel cells, batteries, and supercapacitor. However, this enhanced strategy requires real-time measurement of the vehicle speed for determining the power level processed by the supercapacitor. This enhanced strategy introduces a new control loop designed to maintain the supercapacitor SoC within its operating range, consequently increasing the complexity and stability analysis of the EMS.

On the other hand, the FLC proposed in [20], [25] aimed to keep the primary source operating in its region of optimal efficiency. The disadvantage of this strategy lies on the semi-active topology, where the supercapacitor is directly connected to the dc-link and lacks flexibility to operate it more efficiently. As a consequence, this strategy demands more power from the batteries to regulate the dc-link rated voltage, increasing the effort on these devices.

In the literature, few applications of optimized FLCs have been made in fully active topologies with multiple sources due to the high number of required control parameters and the high computational time for tuning. In semi-active topologies with batteries directly connected to the dc-link, [26], [27] implemented meta-heuristic optimization algorithms for tuning the parameters of FLC based on frequency decoupling. Although the results show reduced fuel consumption and batteries frequency response, they were obtained for specific driving patterns. Additionally, adding another control loop based on frequency decoupling to reduce ESS degradation increases the level of complexity and the number of optimized parameters.

Parallel to the FLC based EMS, sigmoid shaped functions (S-shaped) have been used for different application, as battery energy storage systems SoC equalization and dc-link restoration in dc microgrids [5], [28]. This sigmoid-based method has demonstrated advantages over the FLC, such as ease of parameter tuning and access to the closed-loop model for in-depth stability analysis of the controllers. Consequently, there is a need to investigate an EMS based on these nonlinear functions for HVs, aiming to improve adaptive adjustments without requiring fast communication. The advantage of S-shaped functions include adaptability across different operation conditions, the low number of control parameters required to be tuned and their continuity, which enhances stability in accessing the closed-loop model [5], [28]. Addionally, the S-functions enable the exploration of the fully active topology flexibility, enhancing the use of supercapacitor energy to reduce fuel consumption and battery SoC fluctuations.

Therefore, this paper introduces an EMS based on S-shaped functions for a SHV operating under a fully active topology, comprising an ICE-generator set, batteries, and supercapacitors. The proposed EMS aims to identify disturbances in the dc-link to indirectly determine the power demand for the SHV. This power is then allocated to the ICE and the HESS according to response time and SoC. Consequently, this EMS integrates adaptability and optimization for managing multiple devices (ICE, batteries and supercapacitors) thereby reducing computational burden compared to [8]–[10].

The main advantages of this paper, compared to existing literature, can be summarized as follows:

1) The proposed EMS enables HESS to operate with bidirectional energy flow. It also adds flexibility to operate the sources and enhances the supercapacitors usability;
2) The continuity of the S-functions across their entire domain permit the use of the Lyapunov's indirect method to verify the stability over the entire closed-loop model, evaluating the supercapacitor SoC and dc-link voltage on critical operations in the fully active topology;
3) The controllability of the close-loop model allow the EMS to be applied in meta-heuristic optimization for parameters tuning with reduced number of constraints;
4) The proposed EMS is optimized offline using standard drive cycles to perform in an adaptive manner with easy parameters adjustments.

The paper is organized as follows: Section II presents the fully-active topology description and its control strategy design; Section III presents the proposed EMS; Section V presents the small-signal stability and performance analysis; Section IV presents the EMS parameters tuned by a meta-heuristic optimization; Section IV presents the EMS simulation and experimental results obtained with a low-power prototype used to emulate a SHV, while Section VI presents the conclusion.

Notation: The sets $\mathbb{R}$ and $\mathbb{R}^+$ denotes the set of real numbers and non negative real numbers, respectively.

II. System Description

The architecture SHV is conceived with a fully active electrical powertrain and an EMS control strategy as shown in Fig. 1. The power solution comprises four power units connected to the dc-link to command the energy flow in the electric powertrain (ICE-generator set, HESS, brake resistors and traction motors). The first is the ICE-generator set used as primary source power unit, which is tied to the dc-link via unidirectional dc/dc converter, the second is the battery power unit connected to the same dc-link by a bidirectional dc/dc converter, the third is supercapacitor power unit also using a bidirectional dc/dc converter, and, finally, the over-voltage protection power unit, representing a braking resistor to avoid high levels of voltage on the dc-link during abnormal situations as regenerative braking, transients response, etc. The specific parameters of the main components of the SHV laboratory-scale prototype are defined in Table I.

A. Description of the Electrical Powertrain Structure

The terminal voltages of the primary source and battery terminal voltages are denoted by V_{ps} and V_{bt}, respectively, while the supercapacitor terminal voltage on the capacitance C_{sc} is V_{sc}. The instantaneous currents i_{Lps}, i_{Lbt} and i_{Lsc} are flowing through the primary source inductor L_{ps}, battery inductor L_{bt} and supercapacitor inductor L_{sc}, respectively. The semiconductors S_{ps} and D_{ps} are the primary source semiconductors, S_{1bt} and S_{2bt} are the battery semiconductors while S_{1sc} and S_{2sc} are the supercapacitor semiconductors, activated according the duty-cycles d_{bt}, d_{ps} and d_{sc} by pulse width modulation (PWM).

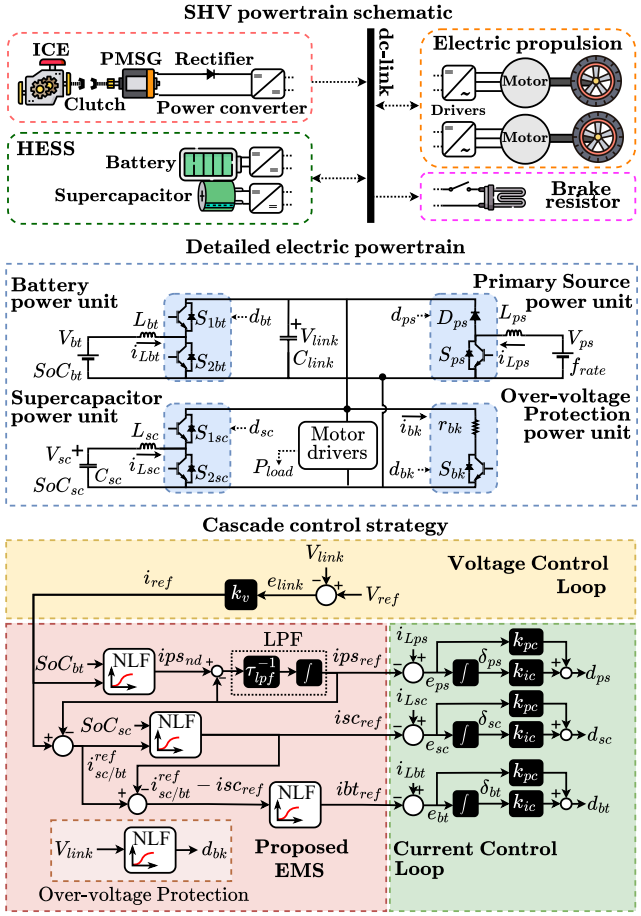

Fig. 1: SHV energy flow, electrical powertrain structure and the control strategy diagram with the proposed EMS. The block non-linear function (NLF) contains S-shaped functions.

TABLE I: Parameters of SHV laboratory-scale prototype.

Component	Parameters	Value
Traction motor (Three phase induction motor)	Rated voltage/current	220 V/0.6 A
	Peak/Rated power	250/125 W@63%*
	Nominal velocity	1,800 rpm
dc-link	max./min. voltage	350/260 V
	C_{link}	1,000 μF
	Useful loads	26 W
Battery	Rated/max. current	0.5 Ah/5 A@10 C
	Nominal voltage	72 V
Supercapacitor	Peak/Rated power	550/100 W
	Rated voltage	100 V
	C_{sc}	0.72 F
Primary source	Rated voltage	60 V
	Max. power	300 W@30%**
	Rated power	72 W@55%**
dc/dc converters	Inductance	4.75 mH
	r_{bk}	200 Ω
	Parasitic losses	0.2 Ω
	Switch frequency	10 kHz

* Motor performance. ** Primary source efficiency.

1) Vehicle load: The dc-link load is produced via a vehicle power P_{load} processed by the motor drivers during the SHV route on the track. At this point of coupling, the voltage V_{link} on the dc-link capacitor C_{link} undergo deviations during maneuvers of load. Thus, considering the high efficiency of the electronic devices used, P_{load} can be calculated by the inertial and aerodynamic drag forces acting on the SHV, as follows:

$$P_{load} = \left(\underbrace{m\dot{v}_t}_{\text{Inertia}} + \underbrace{cv_t^2}_{\text{Drag}} \right) v_t + P_o \tag{1}$$

where m is the mass, c is the aerodynamic drag coefficient, and v_t is the longitudinal speed of the vehicle, while P_o represents the additional power losses of the electrical components.

2) Over-voltage protection: The over-voltage protection power unit consists of a break resistor r_{bk} and a semiconductor S_{bk} activated by the duty-cycle d_{bk}, which was designed to protect the dc-link against over-voltage. The expression governing the power dissipated P_{bk} across r_{bk} is given by

$$\begin{cases} P_{bk} = r_{bk} i_{bk}^2 \\ i_{bk} = r_{bk}^{-1} V_{link} d_{bk} \end{cases} . \tag{2}$$

Therefore, considering that the efficiency of the dc/dc converters is relatively high, the losses that most affect the efficiency of the current electrical topology are inherent to r_{bk} with its current being i_{bk} and activated during dc-link over-voltages.

3) Fuel consumption: The fuel consumption model must accommodate different primary sources as fuel cells and engine-generator set. Therefore, the instantaneous fuel consumption $\dot{f}_{rate}$ is calculated as follows [3], [9]:

$$\dot{f}_{rate} = V_{ps} i_{Lps} b_{ps} \gamma \tag{3}$$

where b_{ps} is the fuel consumption rate and γ is the unit conversion factor. Thus, the primary power source influences the fuel consumption rate as illustrated in Fig. 2a, where the current between its minimum ips_l and maximum ips_u is determined to operate this source within its most efficient range, reducing unnecessary fuel losses.

4) Battery useful life: The battery lifespan is significantly impacted by the increase in its internal impedance, which occurs when battery SoC (SoC_{bt}) is less than 20% or greater than 80%, as well as during high discharge/recharge currents, as illustrated in Fig. 2b. In this context, the SoC_{bt} dynamics

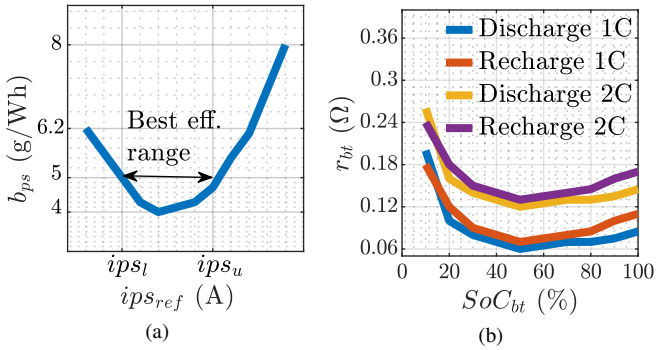

Fig. 2: (a) Fuel consumption rate b_{ps} in terms of ips_{ref}. (b) Batteries r_{bt} varying in terms of SoC_{bt} and Q_{bt}.

should be modeled in terms of the internal resistance of the batteries as follows [3], [9]:

$$\begin{cases} \dot{SoC}_{bt} = -Q_{bt}^{-1} i_{bt}, \\ i_{bt} = \frac{V_{bt} - \sqrt{V_{bt}^2 - 4r_{bt}(V_{bt} i_{Lbt} - i_{Lbt}^2)}}{2r_{bt} Q_{bt}} \end{cases} \tag{4}$$

where Q_{bt} is the battery capacity and r_{bt} is its internal resistance, which varies according to the SoC_{bt}. As r_{bt} becomes more pronounced at both low and high SoC levels, the battery's useful life could be affected under these SoC conditions, increasing heat generation and solid interfaces, which reduce the device's cycle number. [5], [29]. Consequently, these conditions elevates the battery internal temperature, reducing its energy capacity in the long term [29]. Therefore, according to Fig. 2b, maintaining the battery SoC between 50% and 70% could reduce the impact of internal losses, thereby making the use of this component more efficient.

5) Supercapacitor usability: The energy stored by the supercapacitors must be controlled between 50% and 100% for safe and efficient device operation [30], meaning that half of its stored energy is used during cycles discharges to assist other sources. Therefore, the dynamics of the supercapacitor SoC denoted SoC_{sc} must be considered in the closed-loop control structure of the system, defined as

$$\dot{SoC}_{sc} = -\left(C_{sc} V sc_r\right)^{-1} i_{Lsc} \tag{5}$$

where $V sc_r$ is the supercapacitor rated voltage. As observed in (5), SoC_{sc} dynamics depends on i_{Lsc}, and therefore, it must be controlled in the EMS to prevent the device from operating outside its electrical limits.

B. Cascade Control Strategy

The proposed cascade control strategy is shown in Fig. 1 where, in the outer control loop, the disturbance of the dc-link voltage V_{link} around its reference V_{ref} is used to calculate the current reference i_{ref} for all energy devices. Based on the i_{ref}, the EMS defines also the references for each source. Thus, the duty-cycles are calculated in an inner control loop as well.

1) Voltage control loop: The dc-link dynamics is modelled based on the contribution of each power unit and the load as

$$\begin{aligned} \dot{V}_{link} = C_{link}^{-1} \left[i_{Lps} d_{ps} + i_{Lbt} d_{bt} + i_{Lsc} d_{sc} - \right. \\ \left. - r_{bk}^{-1} V_{link} d_{bk} - V_{link}^{-1} P_{load} \right]. \end{aligned} \tag{6}$$

Subsequently, the dc-link voltage control uses a proportional controller to generate the i_{ref} to be distributed among the sources and is calculated as

$$i_{ref} = k_v \underbrace{\left(V_{ref} - V_{link}\right)}_{e_{link}}, \tag{7}$$

where k_v is the proportional gain and V_{ref} is the dc-link voltage reference. To ensure that the control structure operates within its stable region and to prevent overloading of SHV components, the maximum and minimum limits of the V_{link} and i_{ref} must be established in accordance with

$$\begin{cases} V_{min} \leq V_{link} \leq V_{max} \\ i_{min} \leq i_{ref} \leq i_{max} \end{cases}. \tag{8}$$

In order to the sources absorb or supply the total current reference i_{ref}, the battery current reference ibt_{ref}, the supercapacitor current reference isc_{ref} and the primary source current reference ips_{ref} are dynamically defined by the EMS and used in the control loop of current.

2) Current control loop: The inductor current dynamics are modelled as

$$\begin{cases} \dot{i}_{Lps} & = L_{ps}^{-1} \left[V_{ps} - V_{link} d_{ps} \right] \\ \dot{i}_{Lsc} & = L_{sc}^{-1} \left[V_{sc} - V_{link} d_{sc} \right] \\ \dot{i}_{Lbt} & = L_{bt}^{-1} \left[V_{bt} - V_{link} d_{bt} \right] \end{cases}, \tag{9}$$

while the inductor current errors in the current control loop are defined as

$$\begin{cases} e_{ps} & = i_{Lps} - ips_{ref} \\ e_{sc} & = i_{Lsc} - isc_{ref} \\ e_{bt} & = i_{Lbt} - ibt_{ref} \end{cases}, \tag{10}$$

where e_{ps}, e_{sc} and e_{bt} are the primary source, supercapacitor and battery inductor current errors, respectively. Subsequently, the e_{ps}, e_{sc} and e_{bt} are processed by PI controllers to calculate the duty-cycles applied to the semiconductors by using the PWM as

$$\boldsymbol{d} = k_{pc} \dot{\boldsymbol{\delta}} + k_{ic} \boldsymbol{\delta}, \tag{11}$$

where k_{pc} and k_{ic} are the proportional and integral gains, $\boldsymbol{d} = \begin{bmatrix} d_{ps} & d_{sc} & d_{bt} \end{bmatrix}^T$, $\dot{\boldsymbol{\delta}} = \begin{bmatrix} e_{ps} & e_{sc} & e_{bt} \end{bmatrix}^T$ and $\boldsymbol{\delta} = \begin{bmatrix} \delta_{ps} & \delta_{sc} & \delta_{bt} \end{bmatrix}^T$ are defined as the integral of the error $\boldsymbol{e}$. Finally, the current references in (10) are calculated according to the proposed EMS as follows.

III. Proposed EMS

In this section, the EMS is described considering the control strategy diagram shown in Fig. 1. According to the dynamic characteristics of the primary source, batteries and supercapacitor, their current references are calculated as a part of the i_{ref} using S-shaped functions, as detailed in the following sections.

A. Primary Source Management

The primary source current ips_{ref} is calculated with the aim of operating within the region of greater efficiency and with a low time response. The low time response is achieved by using a low-pass filter, which attenuates fast transients during SHV accelerations. Prior to this, the i_{ref} and SoC_{bt} are used to calculate the non-filtered current reference ips_{nd} by using the S-shaped function:

$$ips_{nd} = ips_l + \frac{(ips_u - ips_l)(1 - SoC_{bt})}{1 + e^{\frac{\alpha_1}{i_{max}} \left(\frac{ips_l}{SoC_m} SoC_{bt} - i_{ref} \right)}}, \tag{12}$$

where ips_l is the lower primary source current, ips_u is the upper primary source current, SoC_m is the minimum battery SoC operation, and $\alpha_1 \in \mathbb{R}^+$ is the S-function steepness.

The influence of the SoC_{bt} and the i_{ref} on the ips_{nd} is shown in the surfaces in Fig. 3a for three different α_1 values, along with ips_l and ips_u. These two last parameters must be chosen in accordance with the nominal requirements of the primary source to achieve an efficient operating point, while

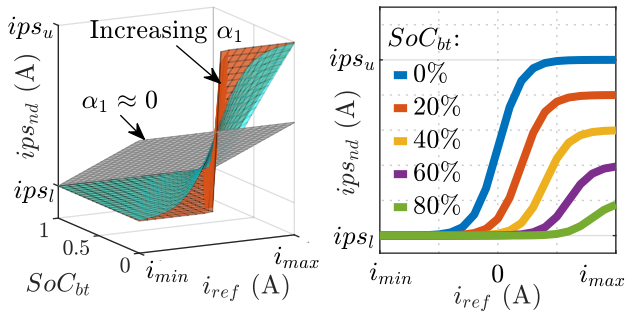

(a) (b)

Fig. 3: (a) ips_{nd} surface given three different α_1. (b) ips_{nd} as a function of i_{ref} for different SoC_{bt} values: 0%, 20%, 40%, 60%, and 80%, respectively, with $SoC_m = 0.2$.

α_1 requires heuristic knowledge to achieve better performance of the primary source. Therefore, a tuning method based on meta-heuristic optimization is necessary to achieve the desired performance in the driving cycle, which will be described in the Section IV.

As observed in Fig. 3a, when $\alpha_1 \approx 0$, the output current ips_{nd} becomes practically constant for each SoC_{bt}, which is not interesting for reaching the best operation during load maneuvers. Thus, by increasing α_1, the desired behaviour of the ips_{nd} is illustrated in Fig. 3b where, for each SoC_{bt}, is visualized that for $i_{ref} << 0$ A (regenerative braking), the ips_{nd} output is defined as ips_l regardless the SoC_{bt} value. For the dc-link discharging process, the current ips_{nd} increases with decreasing SoC_{bt} under load demand, reaching up to the upper value ips_u when $SoC_{bt} = 0\%$. This strategy allows the operation of the primary source to adapt in order to compensate for the SoC_{bt} decrease and avoid the battery deep discharge.

To avoid excessively rapid and high-amplitude responses during the transients in the SHV power demand, the ips_{ref} is calculated filtering ips_{nd} by using a first order low-pass filter (LPF) with time constant τ_{lpf} as

$$\dot{ips}_{ref} = \tau_{lpf}^{-1}(ips_{nd} - ips_{ref}). \tag{13}$$

As the ips_{ref} is defined by the EMS, the remaining current $i_{sc/bt}^{ref} = i_{ref} - ips_{ref}$ required by the dc-link is shared among HESS according to the EMS design.

B. Supercapacitor Management

The supercapacitor is designed to provide power during load maneuvers that occur during rapid vehicle accelerations controlling i_{Lsc} while maintaining SoC_{sc} between 50% and 100%. Thus, to determine the reference isc_{ref}, the S-shaped functions in terms of $i_{sc/bt}^{ref}$ and SoC_{sc} are used as

$$isc_{ref} = \frac{2\alpha_2}{\left(1 + e^{100(0.9 - SoC_{sc})}\right)} - \alpha_2 + \\ + \frac{2\alpha_2}{\left(1 + e^{-\frac{\alpha_3}{i_{max}} i_{sc/bt}^{ref}}\right)\left(1 + e^{100(0.5 - SoC_{sc})}\right)}, \tag{14}$$

where $\alpha_2 \in \mathbb{R}^+$ represents the minimum/maximum current for recharging/discharging the supercapacitor when $0.5 < SoC_{bt} < 0.9$ while $\alpha_3 \in \mathbb{R}^+$ represents the steepness of current processed by the supercapacitor. As observed in (14), the isc_{ref} depends on two parameters, which must be tuned according to the SHV power dynamics used in the meta-heuristic optimization process in Section IV.

As evidenced by the surfaces depicted in Fig. 4a, when $\alpha_3 \approx 0$, the rate of variation in $i_{sc_{ref}}$ in terms of $i_{sc/bt}^{ref}$ is minimal, resulting in low discharge/recharge currents performed by the supercapacitor under load maneuvers. Therefore, such scenario is sub-optimal for leveraging the energy stored. On the other hand, with a very high α_3, the supercapacitor reacts quickly to load transitions, and making the device transfer their storage energy inefficiently or reduce EMS performance during load maneuvers.

Therefore, the desired behavior of the isc_{ref} is illustrated in Fig. 4b, which shows the output current curve for different SoC_{sc} values in terms of $i_{sc/bt}^{ref}$. Notably, when $i_{sc/bt}^{ref} < 0$ A and $0.5 < SoC_{sc} < 0.9$, the isc_{ref} assumes a negative value, indicating the recharging operation mode, with $-\alpha_2$ as minimum current. Conversely, for $i_{sc/bt}^{ref} > 0$ A, the current reference becomes positive, indicating discharging, with the maximum current determined by α_2.

In this solution, the supercapacitor is used to assist the batteries during high current events, while it is charged by the primary source during low load demands. Moreover, when $SoCsc$ is above 90% and below 50%, the supercapacitor is compelled to discharge and recharge, respectively, which ensures that the ESS stays within its voltage operation range, ensuring safe and stable operation. Finally, once the isc_{ref} is defined, the ibt_{ref} can be calculated by the EMS.

C. Battery Management

The difference between $i_{sc/bt}^{ref}$ and the isc_{ref} is used to calculate the ibt_{ref} according the non-linear function

$$ibt_{ref} = \frac{i_{sc/bt}^{ref} - isc_{ref} + ibt_r}{1 + e^{-\frac{100}{i_{max}}\left(i_{sc/bt}^{ref} - isc_{ref} + ibt_r\right)}} - ibt_r, \tag{15}$$

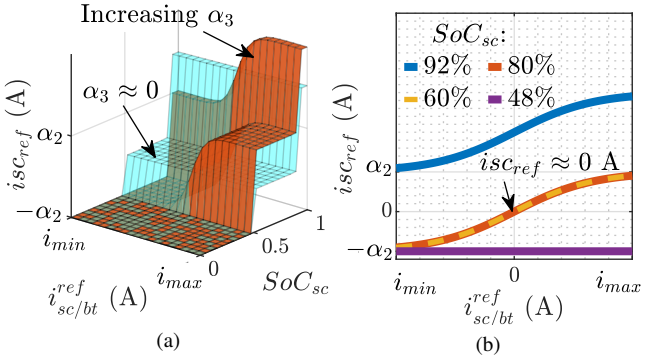

(a) (b)

Fig. 4: (a) Surface to generate isc_{ref} as a function of $i_{sc/bt}^{ref}$ and SoC_{sc} (b) isc_{ref} as a function of $i_{sc/bt}^{ref}$ for different SoC_{sc} values: 48%, 60%, 80%, and 92%.

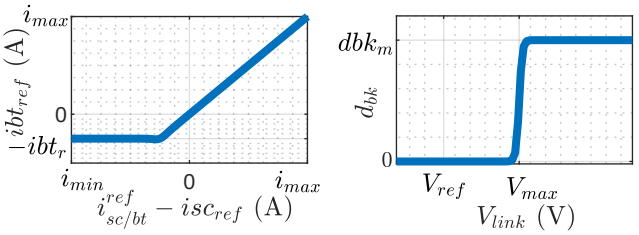

(a) (b)

Fig. 5: (a) ibt_{ref} as a function of the excess power demanded in the dc-link ($i^{ref}_{sc/bt} - isc_{ref}$), (b) d_{bk} duty-cycle as a function of the V_{link} with activation at V_{max}.

where $ibt_r \in \mathbb{R}^+$ is the maximum recharge current that the battery can sustain, which is saturated as a sigmoid curve. As can be seen in Fig. 5a, during recharge the ibt_{ref} is limited to $-ibt_r$ when the dc-link experiences high levels of regenerative power. Therefore, the lower bound ibt_r serves to safeguard the batteries against high current that could lead to over-voltage and overheating during recharging, thereby enhancing its operational lifespan.

D. Over-voltage Protection

The braking resistor acts to protect the SHV from dc-link over-voltages when the HESS are fully charged and a high regenerative power is required. This is achieved by switching-on the semiconductor S_{bk} according to the S-shaped function

$$\begin{cases} d_{bk} = \dfrac{dbk_m}{1 + e^{\frac{100}{V_{ref}}(V_{max} - V_{link})}} \\ dbk_m = \frac{r_{bk} P_{max}}{V^2_{max}} \end{cases} \tag{16}$$

where $dbk_m \in [0\ 1]$ is the maximum duty-cycle, V_{max} is the dc-link maximum operating voltage and P_{max} is the dc-link maximum power. Thereby, the duty-cycle d_{bk} is activated by V_{max} as shown in Fig. 5b.

IV. EMS Tuning by Meta-heuristic Optimization

In this section, the EMS control parameters will be tuned using the meta-heuristic optimization based on the differential evolution algorithm, which is commonly used as meta-heuristic algorithm due its easy implementation. The parameters of tuning are performed offline to ensure that the proposed EMS achieves optimal performance in standard driving conditions, such as those encountered by buses, garbage trucks, and vehicles for cargo or passenger transport. Accordingly, this section discusses three topics: the EMS problem formulation; the differential evolution algorithm used to optimize the main EMS parameters; and the optimization implementation for tuning the EMS.

A. EMS Tuning Problem Formulation

The optimization will aim to reduce fuel consumption and electrical losses while the EMS adapts to keep the SoC_{bt} within a desirable operating range, thereby extending the vehicle driving range and the battery lifespan [3], [9]. Thus, the problem formulation will be based on the expressions governing the fuel consumption rate, battery useful life, and electrical losses inhered by P_{bk}. The electrical losses are calculated to penalizing the optimization process when the EMS guides the sources into a critical region of operation, i.e., when over-voltage activation is forced to act to maintain the stability of the control variables. This significantly increases the energy losses of the overall system and, consequently, the cost function.

The optimization process effectively balances the relationship between fuel savings, battery degradation, and electrical losses. Therefore, the k-th component of a cost function denoted $J_k(\cdot)$ is calculated by the definite integral over the k-th driving cycle time interval $[t_{o_k}\ t_{f_k}]$, with $k \in 1, 2, \ldots, n$ and n the total number of standard cycles. Thus, the cost function $J(\cdot)$ can be expressed by the sum of the J_k for $k = 1, 2, \ldots, n$ as follows:

$$\begin{cases} J_k(\boldsymbol{\alpha_i}) = \int_{t_{o_k}}^{t_{f_k}} \beta_1 \dot{f}_{rate} + \beta_2 i^2_{bt} + \beta_3 P_{bk}\ dt \\ J(\boldsymbol{\alpha_i}) = \sum_{k=1}^{n} J_k(\boldsymbol{\alpha_i}) \end{cases} \tag{17}$$

where β_1, β_2, and β_3 are weighting factors based on the trade-off between fuel savings, battery current stress and electrical losses, and $\boldsymbol{\alpha_i}$ with $i \in i = 1, 2, \ldots, N_{de}$ are the vector of population of parameters to be found in an optimization process. For SHV applications, it is of paramount importance to save fuel for the primary source. Therefore, β_1 is assumed to be greater than β_2 and β_3.

Remark 1. The battery aging is closely related to capacity degradation, which is primarily driven by excessive cycling during charge and discharge processes [29]. As demonstrated in [6], capacity loss is predominantly associated with deep-of-discharge, temperature and charge/discharge rates. Consequently, the reduction of battery current by the term $\beta_2 i^2_{bt}$ in (17) mitigates battery aging reducing discharge rate and heat generated by internal losses. Furthermore, the SoC levels are limited by the primary source power control by the S-function in (12) aiming to improve the battery lifetime. Therefore, the complete battery aging model was not utilized directly because of its intensive computational requirements and the complexity involved in its calibration, making it impractical for applied use [6].

Remark 2. The cost function in (17) involves a trade-off between fuel savings and battery usage in a multi-objective optimization. To address this, the weighting method was employed, where weights are chosen to reflect the relative importance of each objective, as demonstrated in several works in the literature [12], [22], [26], [31], [32]. For each combination of weights, the algorithm identifies the Pareto's front. An alternative approach is the use of the Non-dominated Sorting Genetic Algorithm II, as seen in [33]. However, this method incurs a higher computational cost and offers lower precision in capturing the decision-maker's preferences. In this paper, increasing the value of β_1 results in reduced fuel consumption, while higher β_2 values lead to a decrease in battery current.

B. Differential Evolution Algorithm

In what follows, an heuristic approach is used to search for the S-shape parameters denoted by vector $\boldsymbol{\alpha}_{i,g}$ with $i = 1, 2, ..., N_{de}$ with N_{de} the number of trials and g the index for each EMS parameters to be tuned in (12) and (14) ($g = 1, 2, 3$). Each $\boldsymbol{\alpha}_{i,g}$ has the following constraints:

$$\begin{aligned} \boldsymbol{\alpha}_{i,g} &= \left[\alpha_{i,1}\ \alpha_{i,2}\ \alpha_{i,3}\right]^T, \\ \text{s.t.} &\begin{cases} 0 \leq \left[\alpha_{i,1}\ \alpha_{i,3}\right] \leq 10 i_{max} \\ 0 \leq \alpha_{i,2} \leq i_{max} \end{cases} \end{aligned} \tag{18}$$

with the maximum value of $\alpha_{i,1}$ and $\alpha_{i,3}$ chosen according to the maximum S steepness in (12) and (14), respectively, while the maximum $\alpha_{1,2}$ is given by the maximum external-loop reference. The remaining EMS parameters are fixed and determined based on the electrical specifications of the powertrain components.

Given the constraints and fixed parameters, the differential evolution algorithm initialize with the most promising candidates. Then, the mutant vector calculation is performed as follows [34], [35]:

$$\boldsymbol{\psi}_{i,g} = \boldsymbol{\alpha}_{r_1,g} + \boldsymbol{\mu}_{de}\ (\boldsymbol{\alpha}_{r_2,g} - \boldsymbol{\alpha}_{r_3,g}) \tag{19}$$

where $\boldsymbol{\psi}_{i,g}$ represents the mutant vector, $r_1,\ r_2,\ r_3 \in 1, 2, \ldots, N_{de}$ are random integers, and $\boldsymbol{\mu}_{de}$ is the scaling factor in the range $[0, 2]$. Then, the crossover of the mutant candidates with the current ones generates the trial candidates, calculated by each g as follows [34], [35]:

$$\boldsymbol{\xi}_{i,g} = \begin{cases} \boldsymbol{\psi}_{i,g} \text{ if } rand(0,1) < c_r \text{ or } g = g_r \\ \boldsymbol{\alpha}_{i,g} \text{ otherwise} \end{cases} \tag{20}$$

where $rand\,(\cdot)$ is the random operator, $g_r \in 1, 2, \ldots, N_{de}$ is a random integer vector and c_r is the crossover probability. Finally, the selection of individuals for the next iteration (it) is done by comparing the trial vector $\boldsymbol{\xi}_{i,g}$ and their parental solutions $\boldsymbol{\alpha}_{i,g}$ in the current population as follows [34], [35]:

$$\boldsymbol{\alpha}_{i,g}^{it+1} = \begin{cases} \boldsymbol{\xi}_{i,g} \text{ if } J(\boldsymbol{\xi}_{i,g}) < J(\boldsymbol{\alpha}_{i,g}) \\ \boldsymbol{\alpha}_{i,g} \text{ otherwise} \end{cases} \tag{21}$$

with $J\,(\cdot)$ the cost function calculated at each population of N_{dc} generated as in (17).

The termination criterion for the algorithm can be defined based on the cost value or the maximum number of iterations. After the optimization process has been completed, the best candidates can be stored for reuse in a new tuning to re-adapt the EMS to new driving or operating conditions.

C. EMS Optimization and Tuning Process

The parameters that most impact the performance of the EMS are tuned based on a cost function minimization. The diagram illustrated in Fig. 6 outlines the procedures for optimizing and tuning the EMS using the differential evolution algorithm. Briefly, the meta-heuristic algorithm evaluates N_{de} new trial groups by the cost function, subsequently generating new mutants and performing crossover at each iteration.

The cost function receives the trial vectors $\boldsymbol{\xi}_i$ with $i \in i = 1, 2, \ldots, N_{de}$ and the selected power demands P_{load}^k with $k \in k = 1, 2, \ldots, n$, which are extracted from a dataset containing the power consumption performed by SHV laboratory-scale prototype during Dallas repeated driving cycles [36]. Thus, for each i, the closed-loop model of the EMS is executed for k power demands, where J_k is calculated based on data $\dot{m}f$, i_{bt}, and P_{bk} extracted from the simulated model. The cost J_k is then added to J_i for each $\boldsymbol{\xi}_i$.

The ordinary differential equations (ODEs) of the closed-loop model are solved by MATLAB over the time interval $[t_{o_k}\ t_{f_k}]$ for each P_{load}^k. Since the developed model is controllable, it is suitable for application in a meta-heuristic optimization strategy for tuning the parameters of the EMS offline. This eliminates the need to provide further constraints related to the electrical specifications and operation limits of the system.

Therefore, the process combines the optimization and adaptability of the EMS in different operational conditions using a lower number of constraints. Additionally, initializing the differential evolution algorithm with the best candidates enhances its convergence speed, making it promising for real-time adaptation to various driving or operation conditions with different sources combinations. For this initial training, the time elapsed for tuning the parameters was 1,714 s (28.57 min), with the control and differential evolution parameters indicated in Table II.

V. EMS Stability and Performance

In this section, the stability and performance analysis of the SHV laboratory-scale prototype is conducted considering the proposed EMS under the cascade control. The evaluation involves the SHV nonlinear model, and the stability analysis of eigenvalues using Lyapunov's indirect method as in [5], [28], while performance is evaluated by using the $\mathcal{H}_\infty$ norm as in [28]. Therefore, the following remarks and assumptions are given.

Remark 3. Considering the dynamic response of SoC_{bt} to be much slower than the other storage elements in the control structure, $\dot{SoC}_{bt} = 0$ is assumed and will be neglected in the stability analysis.

Remark 4. The instantaneous fuel consumption $\dot{m}_f$ does not impact the dynamics of the control variables, thus not affecting the stability of the EMS.

TABLE II: Fixed control parameters, differential evolution parameters and the best $\boldsymbol{\alpha}$ found.

Fixed control parameters					
Par.	Value	Par.	Value	Par.	Value
V_{ref}	310 V	k_v	0.08 A.V^{-1}	i_{max}	4 A
τ_{lpf}	4 s	ips_l	0.6 A	ips_u	3 A
ibt_r	1 A	P_{max}	250 W	V_{max}	350 V
k_{pc}	0.1 A^{-1}	k_{ic}	0.2 A^{-1}.s	SoC_m	20%
Differential evolution parameters					
Par.	Value	Par.	Value	Par.	Value
β_1	5	β_2	1	β_3	1
N_{de}	20	n	3	Iteration	20
Best candidates found					
Par.	Value	Par.	Value	Par.	Value
α_1	20.4	α_2	0.9 A	α_3	8.4

*Algorithm time execution: 1.714 s

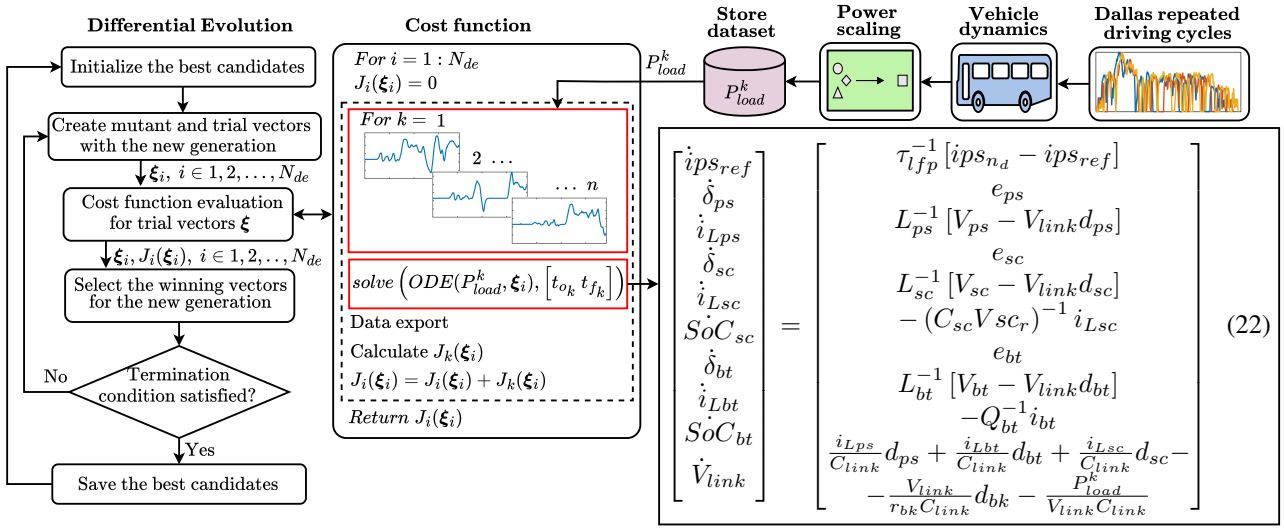

Fig. 6: Differential evolution optimization for tuning the EMS parameters and ODEs representation.

Assumption 1. Considering the circuit and controller parameters are known, the constant load power P^*_{load} is changed point by point affecting the equilibrium voltage denoted V^*_{link}, where $V^*_{link} \geq V_{bt}$. Consequently, $i^*_{ref} = k_v\left(V_{ref} - V^*_{link}\right)$. Therefore, state-feedback controllers are proposed to keep the closed-loop system at the equilibrium points making the states $\boldsymbol{x^*} = [ips^*_{ref}\ \delta^*_{ps}\ i^*_{Lps}\ \delta^*_{sc}\ i^*_{Lsc}\ SoC^*_{sc}\ \delta^*_{bt}\ i^*_{Lbt}\ V^*_{link}]$ (locally) asymptotically stable in the domain of attraction.

Assumption 2. The SoC_{sc} must be analyzed at the equilibrium points where its operation is at a minimum (50%) and maximum (90%). The stability of SoC_{sc} at these equilibrium points is crucial to ensure the safe operation of this device. Thus, when $\dot{SoC}_{sc} \approx 0$, then $isc_{ref} \approx 0$ and

$$SoC^*_{sc} \approx \begin{cases} 0.9, & i^{ref}_{sc/bt} \leq 0 \\ 0.5, & i^{ref}_{sc/bt} > 0 \end{cases}. \tag{23}$$

Assumption 3. As a PI controller is used at low levels, the inductor currents must track the reference at steady-state regime with a settling time one decade shorter than that calculated by the EMS. Therefore, fixing $e_{ps} = 0$, $e_{sc} = 0$ and $e_{bt} = 0$, the inductor currents at the equilibrium point are given by

$$\begin{cases} ips^*_{ref} = ips_{nd}(SoC_{bt}, i^*_{ref}) \\ i^*_{Lps} = ips^*_{ref} \\ i^*_{Lsc} = 0 \\ i^*_{Lbt} = ibt_{ref}(i^*_{Lps}, i^*_{Lsc}, i^*_{ref}) \end{cases}. \tag{24}$$

Subsequently, using the thirty, fifty and eighty equations line of (22) (see Fig. 6) , $\boldsymbol{\delta^*}$ are given by

$$\begin{cases} \delta^*_{ps} = \frac{V_{ps}}{k_{ic} V^*_{link}} \\ \delta^*_{sc} = \frac{V_{sc}}{k_{ic} V^*_{link}} \\ \delta^*_{bt} = \frac{V_{bt}}{k_{ic} V^*_{link}} \end{cases}. \tag{25}$$

Taking into account Remark 1 and the equilibrium points in (23), (24) and (25) of the closed-loop model, (22) can be linearized employing the small-signals analysis with $\boldsymbol{F(x, u)} \in \mathbb{R}^{9\times 1}$ the ODEs of the closed-loop in (22), with $\boldsymbol{x} = [ips_{ref}\ \ \delta_{ps}\ \ i_{Lps}\ \ \delta_{sc}\ \ i_{Lsc}\ \ SoC_{sc}\ \ \delta_{bt}\ \ i_{Lbt}\ \ V_{link}]^T$ and $u = P_{load}$.

The linearized $\boldsymbol{F}(\boldsymbol{x}, u)$ around $(\boldsymbol{x^*}, u^*)$ for small variations denoted $(\hat{\boldsymbol{x}}, \hat{u})$ is thus obtained considering the following series Taylor approximation:

$$\begin{cases} \boldsymbol{f}(\hat{\boldsymbol{x}} + \boldsymbol{x}^*, \hat{u} + u^*, t) \approx \boldsymbol{F}(\boldsymbol{x}^*, u^*, t) + \boldsymbol{A}\hat{\boldsymbol{x}} + \boldsymbol{b}\hat{u} \\ \boldsymbol{A} = \nabla_{\boldsymbol{x}} \boldsymbol{F}(\boldsymbol{x}, u)|_{(\boldsymbol{x},u)=(\boldsymbol{x^*},u^*)} \\ \boldsymbol{b} = \dfrac{\partial \boldsymbol{F}(\boldsymbol{x}, u)}{\partial P_{load}}|_{(\boldsymbol{x},u)=(\boldsymbol{x^*},u^*)} \end{cases} \tag{26}$$

with $\nabla_{\boldsymbol{x}}(\cdot)$ the gradient operator. Finally, the EMS output is defined as $\boldsymbol{y} = [i_{Lps}\ \ i_{Lsc}\ \ SoC_{sc}\ \ i_{Lbt}\ \ SoC_{bt}\ \ V_{link}]^T$, which is used for the feedback control, graphical analysis and for obtaining the transfer functions for the $\mathcal{H}_\infty$ norm analysis.

A. Lyapunov's Indirect Method for Stability Analysis

The Lyapunov's indirect method uses $\dot{\hat{\boldsymbol{x}}} = \boldsymbol{A}\hat{\boldsymbol{x}}$ (with $\hat{\boldsymbol{u}} = 0$) to analyze the local stability of the closed-loop system.

1) Local stability on operating zone: In the first analysis shown in Fig. 7a, the equilibrium points were obtained with SoC_{bt} of 20% and 80% while the load varying from -260 to 260 W, which is the safe operating range. During regenerative mode, at power levels below -56 W, the batteries limit their current supply to $-ibt_r$ while the primary source is forced to work with a minimum current injection of ips_l. Additionally, the equilibrium points of SoC^*_{sc} and V^*_{link} converge to their maximum limits of 90% and V_{max}, respectively. Thus, the overall analysis reveals that $\max(\mathbb{R}_{\lambda_i}) = -0.25$, determined by the dominance of the slowest pole of the LPF, i.e., $-\tau^{-1}_{lpf}$.

Above -56 W, the equilibrium points indicate that the batteries were able to supply the excess of current demanded by the load $i^{ref*}_{sc/bt}$. Thus, the V^*_{link} is decreased and controlled by the proportional gain k_v while the primary source is taken

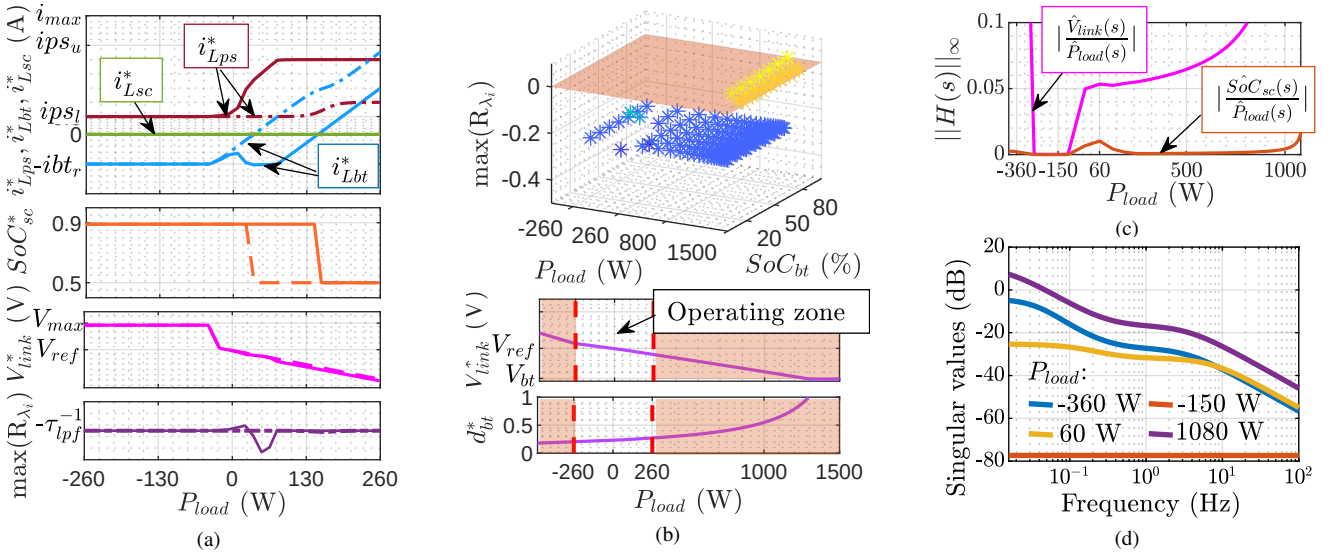

Fig. 7: Stability and performance analysis. (a) Represent the steady-state equilibrium of i^*_{Lps}, i^*_{Lbt}, i^*_{Lsc}, SoC^*_{sc}, and V^*_{link} point by point with the load varying from -260 to 260 W, and the maximum real eigenvalue obtained from matrix $\mathbf{A}$: $SoC_{bt} = 20\%$ (continuous line) and $SoC_{bt} = 80\%$ (dashed line). (b) Effects of SoC_{bt} with load on the maximum real term of the eigenvalues and the steady-state equilibrium points of V^*_{link} and d^*_{bt} for each constant load. (c) Infinity norm analysis for each equilibrium points varying P_{load} from -360 to 260 W point by point. (d) Maximum singular values of $H(s)$ for -360 W, -150 W, 60 W and 1080 W constant load.

to increase its current injection according to (12). In this interval, the equilibrium point of SoC_{sc} transitions to its minimum threshold of 50% when $i^*_{Lbt} > 0$ A, demanding HESS power assistance to the primary source. It is observed from the equilibrium points obtained with $SoC_{bt} = 20\%$ that the primary source injects a higher power level, and the batteries recharge across a wider charge range. Conversely, when $SoC_{bt} = 80\%$, the batteries discharge earlier to compensate the load's power demand and requiring less fuel consumption from the primary source. Thereby, for both analyzed SoCs, $\max(\mathbb{R}_{\lambda_i}) = -0.20$.

Remark 5. Over the load interval analysed, the equilibrium point of i^*_{Lsc} was zero, as at the analyzed equilibrium points (50% and 90% SoC), the requested current must be negligible to limit the output SoC_{sc}.

Remark 6. Since $V^*_{link} \geq V_{bt}$ and considering Assumption 2, the matrix $\boldsymbol{A}$ contains non-zero elements in all columns. However, for values of de $0.5 < SoC^*_{sc} < 0.9$ at equilibrium points that result in $isc_{ref} \approx 0$, the sixth column of the matrix $\boldsymbol{A}$ where $\frac{\partial \boldsymbol{F}(\boldsymbol{x},u)}{\partial SoC_{sc}}|_{(\boldsymbol{x},u)=(\boldsymbol{x}^*,u^*)}$ will contain all zero elements. This result implies that the closed-loop system approaches marginal stability with eigenvalue at the origin. Therefore, the responses of SoC_{sc} in these scenarios do not return to their initial condition.

2) Local stability on critical operations: The second analysis of the $\max(\mathbb{R}_{\lambda_i})$ was performed considering the variation of the SoC_{bt} from 20% to 80% and the load from -300 to 1,500 W. As shown in Fig. 7b, the behavior of $\max(\mathbb{R}_{\lambda_i})$ was not positive in all combinations of SoC_{bt} and load demand higher than 1,000 W. The occurrence of this is illustrated by the equilibrium points of V^*_{link} and $d^*_{bt} = \delta^*_{bt} k_{ic}$, where high load demand caused a significant drop in V_{link} and consequently saturated d_{bt}, rendering it incapable of operating the battery's dc/dc converter. However, this instability-prone operation is far from the unsafe operating zone of the dc-link, which ensures reliability in the practical implementation of the proposed EMS.

B. $\mathcal{H}_\infty$ Norm for Performance Analysis

The $\mathcal{H}_\infty$ norm is used to analyze the attenuation performance of $\hat{V}_{link}$ and $\hat{SoC}_{sc}$ with respect to the load disturbance defined as $\hat{P}_{load}$. The gain output of $\hat{V}_{link}$ and $\hat{SoC}_{sc}$ with respect to $\hat{P}_{load}$ was evaluated using the transfer function matrix denoted $\boldsymbol{H}(s) \in \mathbb{R}^{2\times 1}$ calculated by

$$\boldsymbol{H}(s) = \boldsymbol{C}\left(s\boldsymbol{I} - \boldsymbol{A}\right)^{-1}\boldsymbol{b} \tag{27}$$

where $\boldsymbol{C} = \begin{bmatrix} 0&0&0&0&0&1&0&0&0 \\ 0&0&0&0&0&0&0&0&1 \end{bmatrix}$, $\boldsymbol{A}$ and $\boldsymbol{b}$ the linearized system, and $\boldsymbol{I} \in \mathbb{R}^{\mathbf{9\times 9}}$ the identity matrix.

Considering the load P_{load} varying from -360 to 1080 W, the $\mathcal{H}_\infty$ norm of (27) defined in terms of the frequency-dependent singular values is shown in Fig. 7c. For power demands lower than -350 W and higher than 1000 W, the norm of $\hat{V}_{link}$ in relation to $\hat{P}_{load}$ increases, indicating higher sensitivity of the EMS when the braking resistor is unable to stabilize the maximum dc-link voltage V_{max} or d^*_{bt} is saturated. The opposite occurs when the braking resistor protect the dc-link against overvoltage, as seen for power demands from -350 to -60 W where the norm approaches zero, indicating higher attenuation, that is, disturbances in $\hat{P}_{load}$ do not significantly affect $\hat{V}_{link}$ or $\hat{SoC}_{sc}$. Finally, the norm increases slightly above -90 W when the over-voltage protection is not triggered and the dc-link is regulated by the

proportional gain, indicating a small increase in the sensitivity of $\hat{V}_{link}$ and SoC_{sc} to $\hat{P}_{load}$.

Furthermore, it was observed that the $\mathcal{H}_\infty$ norm of $\hat{SoC}_{sc}$ in relation to $\hat{P}_{load}$ is attenuated for demands below -100 W and above 130 W, indicating low sensitivity of $\hat{SoC}_{sc}$ to additional $\hat{P}_{load}$ events. This behavior is favorable to ensure that SoC_{sc} remains unaffected under both low and high load demands.

For demands between -60 W and 130 W, the sensitivity of $\hat{SoC}_{sc}$ is more affected, especially when isc_{ref} intersects zero as shown in Fig. 7a. In this condition, the supercapacitor may need to discharge or recharge in response to a disturbance $\hat{P}_{load}$ and the slope level α_3. However, the increase in the norm was not sufficient to affect the output $\hat{SoC}_{sc}$.

As illustrated in Fig. 7d, the singular value analysis using the transfer function matrix $H(s)$ in (27) was conducted for equilibrium points with a constant load of -360 W, -150 W, 60 W and 1080 W. In this regard, the singular values exhibited a maximum attenuation of -4 dB at low frequencies for $P_{load} = -350$ W, -77 dB for $P_{load} = -150$ W, -25 dB for $P_{load} = 60$ W and 10 dB for $P_{load} = 1080$ W. In this way, $||\boldsymbol{H}(s)||_\infty \leq 3$ for the P_{load} values analyzed, giving the impression that the closed-loop model amplifies the vehicle load disturbances. However, this result occurs for high load demands, i.e., outside the EMS operating zone. Thus, for operating range of the closed-loop model from -260 to 260 W (operating zone), the singular values indicated effective attenuation against vehicle load disturbances.

VI. Simulation and Experimental Results

In this section, simulations and experiments results are conducted to evaluate the performance of the EMS based on S-shaped functions, with the parameters obtained from Table II. To verify the versatility of the proposed EMS, six urban driving cycles were collected and processed to serve as test scenarios: the new cycle in Dallas retrieved from [36]; Port Drayage local cycle (PDL), Orange County transit bus cycle (California) (OCT), New York bus composite cycle (NYC), collected from the National Renewable Energy Laboratory [37]; and New European (NEDC) and Artemis urban cycle (AUC). Meanwhile, to assess the effectiveness of the proposed EMS, an optimal approach based on the Pontryagin's minimum principle (PMP) [38], a fuzzy logic controller as in [20], and an FLC combined with Haar Wavelet transform (FLC+HWT) as in [21] were adopted as comparative methods.

The Dallas, PDL, NYC, and AUC driving cycles used in the simulation results are illustrated in Fig. 8. These cycles were selected for their similar driving profiles, characterized by urban environments with traffic lights and city blocks. The power demand of the SHV laboratory-scale prototype was extracted corresponding to each driving cycle. Therefore, for a fair analysis, the strategies chosen for comparison (FLC and FLC+HWT) were reconfigured to meet the same power demand as the prototype under its topologies with multiple sources connected to the dc-link (primary source, batteries, and supercapacitors). Finally, the PMP was adopted as the optimal benchmark strategy in this study because it is fast, effective, and comparable to optimization techniques based on dynamic programming (DP) [23].

A. Simulation Results

Fig. 9 illustrates the results for the power transferred from the primary source and the batteries, as well as the supercapacitors and batteries SoCs during a new Dallas driving cycle. Among the S-shaped, FLC and FLC+HWT there are notable differences in how the sources are operated. The results indicate that the FLC required more power from the primary source, consequently increasing the effort on the battery with frequent recharging current, where the SoC_{bt} surpassed 80%, which is above the maximum safe operating limit of the component. Meanwhile, although the FLC+HWT strategy reduces the fluctuation of SoC_{bt}, it demands more power from the primary source to supply the SHV load. Consequently, the electrical losses related to the dc/dc converter of this source are higher, which affect the overall system efficiency. Additionally, the energy stored by the supercapacitors in both the FLC and FLC+HWT strategies was less utilized, as evidenced by the low fluctuation of SoC_{sc} compared to the S-shaped and PMP results.

Regarding the proposed S-shaped based EMS, the energy from the supercapacitors was better utilized, following a dynamic similar to the optimal approach from the PMP. This was achieved due to the ability of the S-shaped functions to adjust the supercapacitor current reference to meet the SHV power demand. Consequently, the proposed EMS required less power from the primary source and the batteries, with greater assistance from the supercapacitors. This proved to be more effective than the FLC and FLC+HWT methods in reducing fluctuations in the SoC of the batteries, saving fuel, and enhancing the driving range of the SHV.

The results of the battery SoC are shown in Fig. 10 where, the SoC curve obtained from the FLC strategy evidenced a high recharge rate across all analyzed driving profiles, indicating low battery utilization and inefficient fuel consumption from the primary source. Additionally, although the FLC+HWT strategy exhibited low fluctuation relative to

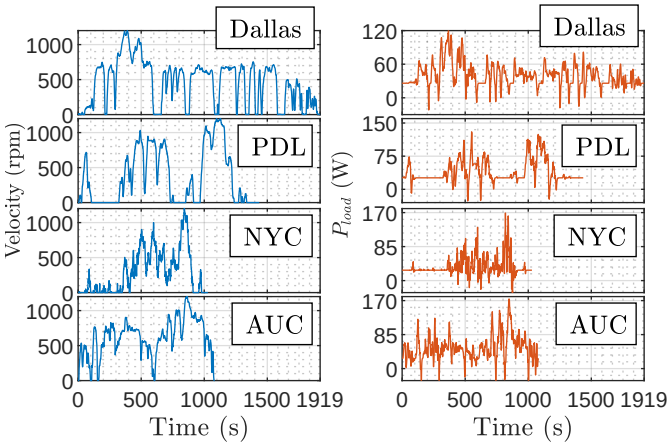

Fig. 8: Velocity and SHV low-scale prototype power demand during Dallas, PDL, NYC, and AUC driving cycles.

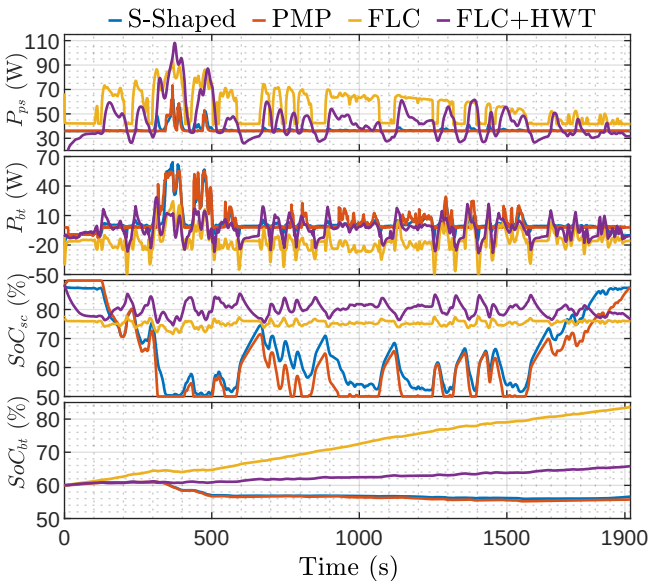

Fig. 9: Power sharing and SoC comparisons among proposed EMS, PMP, FLC and FLC+HWT during Dallas driving cycle.

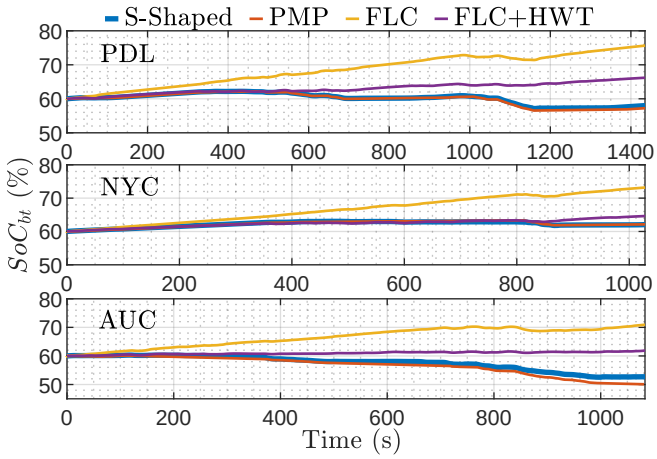

Fig. 10: SoC_{bt} variations of different EMS strategies during the simulation test in PDL, NYC and AUC.

the initial SoC, it resulted in higher fuel consumption to compensate for the SHV power demand, consequently leading to greater overall system losses (fuel and electrical power). In contrast, the SoC curve obtained from the proposed EMS showed lower fluctuation and recharge rate, reflecting reduced battery stress compensated by the assistance of the supercapacitors. Consequently, the SoC dynamics with the EMS based on S-shaped functions closely resembled the dynamics obtained by the optimal approximation made by the PMP, lending credibility to the proposed method.

To evaluate the effectiveness and adaptability of the proposed EMS in different driving scenarios, new results were collected using the tuned parameters from Table II. The quantitative results are presented in Table III, which assess fuel consumption, battery SoC relative error, overall losses, overall efficiency, and the cost function result from (17). The results demonstrate that the EMS based on S-shaped functions outperforms both the FLC and FLC+HWT in terms of fuel economy and electrical losses. The relative error in relation to 60% of the SoC_{bt} was less than 5% in all analyzed scenarios, with only small differences between the results obtained by PMP and FLC+HWT. This demonstrates that the proposed EMS is capable of maintaining battery operation at an efficient power rate while significantly reducing fuel consumption. Furthermore, the proposed EMS consistently shows average results closer to the PMP. This quantitatively highlights how the proposed EMS results that resemble the optimal approximation method adopted.

B. Experimental Results

The validation of the proposed EMS was conducted using a SHV laboratory-scale prototype, as illustrated in Fig. 11. To emulate the wheel load of the vehicle on the powertrain, two pairs of three-phase induction machines (TIMs) from Table I were coupled. In one pair, one TIM operates as traction under closed-loop vector control and the other TIM operates as vehicle inertia and aerodynamic resistance under open-loop voltage/frequency control. In this context, the dSPACE acts as the vehicle control unit, computing the vehicle driving cycle and communicating with the TIMs drivers via analog signals. Analog signals are converted into longitudinal velocity references for the traction TIMs (v_{tr}) and the resistance TIMs (v_{rs}), where the difference in speeds determines the slip and torque applied by the traction machine (T_{tr}). Thereby, when the v_{rs} is lower than the v_{tr}, power is consumed, while the opposite behavior produces regenerative power, as given by

$$\begin{cases} P_{load} \propto T_{tr} v_{tr} \geq 0, & v_{tr} \geq v_{rs} \\ P_{load} \propto T_{tr} v_{tr} < 0 & v_{tr} < v_{rs} \end{cases} . \tag{28}$$

Thus, v_{rs} can be determined in terms of v_{tr} and the vehicle dynamics equations presented in [21] and [6] as follows:

$$v_{rs} = v_{tr} - \underbrace{j\dot{v}_{tr}}_{\text{inertia}} - \underbrace{c v_{tr}^2}_{\text{drag}} \tag{29}$$

$$\text{where} \quad j = \begin{cases} j_a, & \text{if } \dot{v}_{tr} \geq 0 \\ j_d, & \text{if } \dot{v}_{tr} < 0 \end{cases} ,$$

with j_a and j_d defined as vehicle inertia acceleration and inertia deceleration, respectively. Therefore, the prototype bench is able to emulate the same SHV dynamic characteristics in low-scale limited by the maximum TIM powers.

Similarly, to emulate the primary source and supercapacitor, two bidirectional programmable sources were employed, which are configured according to these sources electrical and dynamic specifications presented in Table I. Furthermore, a bank of six lead-acid batteries working as the primary energy storage is used, with its SoC calculated by (4) using Coulomb's counting method. As illustrated in Fig. 1, all three sources are connected to the dc-link via bidirectional boost converters, with the load generated by the traction TIM drivers. Additionally, the over-voltage protection is provided by the braking resistor using analog and switch devices. The host computer compiles the vehicle driving cycles, the EMS, and the controllers on the dSPACE, observes the running status

TABLE III: Quantitative comparison results of different EMS methods.

Cycles		EMS method	Fuel consumption (g)		Fuel consumption. increase (%)		SoC_{bt} relative error (%)*		Overall losses (Ws)		Overall efficiency (%)		Cost function	
Dallas	PDL	PMP	132.8	100.2	[-]	[-]	5.44	2.49	[-]	[-]	[-]	[-]	717.9	564.8
		S-shaped	134.2	101.2	1.04	1.01	4.75	2.19	186.4	151.0	99.75	99.73	720.3	566.6
		FLC+HWT	146.8	113.4	10.4	13.2	4.22	5.06	243.3	209.4	99.67	99.63	772.9	603.8
		FLC	175.0	127.9	31.7	27.6	19.81	14.18	380.9	274.4	99.49	99.51	1012.0	750.6
NYC	AUC	PMP	71.0	77.3	[-]	[-]	2.94	5.58	[-]	[-]	[-]	[-]	374.2	460.1
		S-shaped	72.0	80.8	0.24	4.4	3.66	4.10	98.8	148.8	99.72	99.73	378.8	474.8
		FLC+HWT	74.8	88.6	4.1	14.5	4.11	1.63	119.3	169.9	99.66	99.65	398.3	466.3
		FLC	88.5	110.1	23.2	42.5	11.22	10.91	179.6	288.7	99.51	99.47	522.7	665.4

*The SoC_{bt} relative error was in reference to 60% of the initial condition adopted.

signals in real-time from the current and voltage sensors, and stores the experimental data. Finally, the dSPACE device has digital output channels that are used to control the dc/dc converters via pulse-width modulation (PWM).

1) Comparison between the experimental results and the analytical model: The performance of the EMS and the dynamic behavior of the controlled variables were validated comparing the experimental results (continuous line) with the analytical solution (dashed line) obtained by solving the ODEs presented in (22) using MATLAB® and Simulink®. For this purpose, the NEDC and OCT driving cycles was applied during 600 s, extracting the load power by the action of the traction TIM coupled to the resistance TIM. The dynamics of v_{tr} and v_{rs} of the TIMs shown in Fig. 12a and 12b were obtained according to (29). Using $j_d > j_a$, it is observed that v_{rs} becomes greater than v_{tr} during decelerations, forcing the traction TIM to brake more sharply and regenerate more power. During accelerations, v_{rs} is slightly less than v_{tr}, resulting in moderate power consumption from the dc-link, which increases at higher cruising speeds. Thus, the power drawn from the dc-link (P_{load}) exhibited behavior similar to vehicle dynamics models found in the literature [6], [21].

As shown in Figs. 12a and 12b, the experimental and simulation results exhibited similar dynamic behaviors. The differences observed are mainly due to approximations made in (22) and sensor errors of 2%. The similar responses corroborate the reliability of the ODEs in (22) for application in meta-heuristic optimization methods and the theoretical stability analysis presented in this work. Therefore, the analytical model is suitable for further study through hardware-in-the-loop tests of new control methods with EMS applied in SHVs fully active topologies.

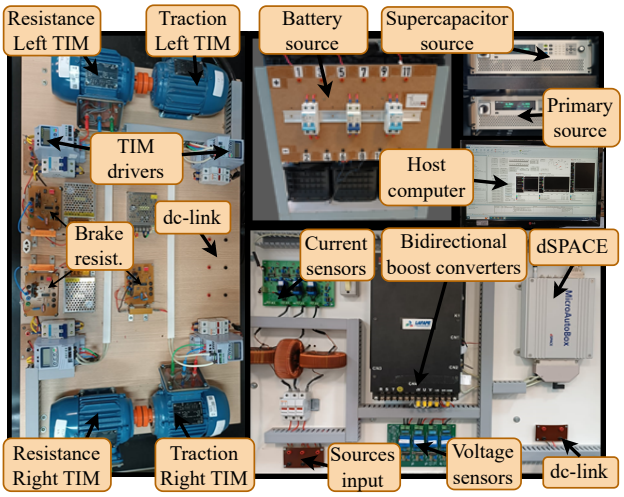

Fig. 11: SHV low-scale prototype and test bench.

2) Comparison between the experimental results and the optimal approach method: In order to evaluate the effectiveness of the proposed EMS in real scenarios, the optimal approach by PMP was applied using P_{load} extracted from the experimental tests. The EMS based on S-shaped functions showed performance relatively close to that calculated by PMP, with reduced fuel consumption and relative SoC_{bt} error on both NEDC and OCT.

To illustrate the comparison more intuitively, the quantitative results of the experiment and the PMP are shown in Table IV. In NEDC and OCT, the error between fuel consumption by the S-shaped method relative to the PMP was 2.58% and 1.33%, respectively, indicating that the consumption obtained in practice approximated the optimized result. However, the relative SoC_{bt} error was more pronounced in NEDC using the S-shaped method (14,6% error). Although the higher SoC_{bt} error is related to increased battery usage and reduced fuel consumption, it is observed that the supercapacitors were not optimally utilized compared to the PMP results. This behavior can be attributed to the increased power after 200 s of the NEDC cycle, characterized by highway driving conditions, which differ from the urban driving profile of Dallas used for EMS parameter tuning. For example, on highways, the vehicle reaches higher cruising speeds with intense braking, whereas in urban areas, vehicles reach lower cruising speeds and brake more frequently at speed bumps, traffic lights, and intersections. Consequently, the standardization of driving profiles has a significant impact on the extent of supercapacitor utilization and achieve a good trade-off between fuel consumption and battery stress.

Overall, the practical results showed optimized fuel consumption and moderate battery usage in urban driving cycle as proven by the OCT test. This confirms that the proposed EMS can be suitable for real-time applications with only offline tuning. Additionally, the S-shaped EMS has the potential to improve results through online readjustment of parameters with lower computational cost due to the reduced number of control parameters. The complex real world applications may exhibit different driving patterns within a given time interval. This implies the needed to identify these patterns and adjust the EMS gains to accommodate the desired driving scenario,

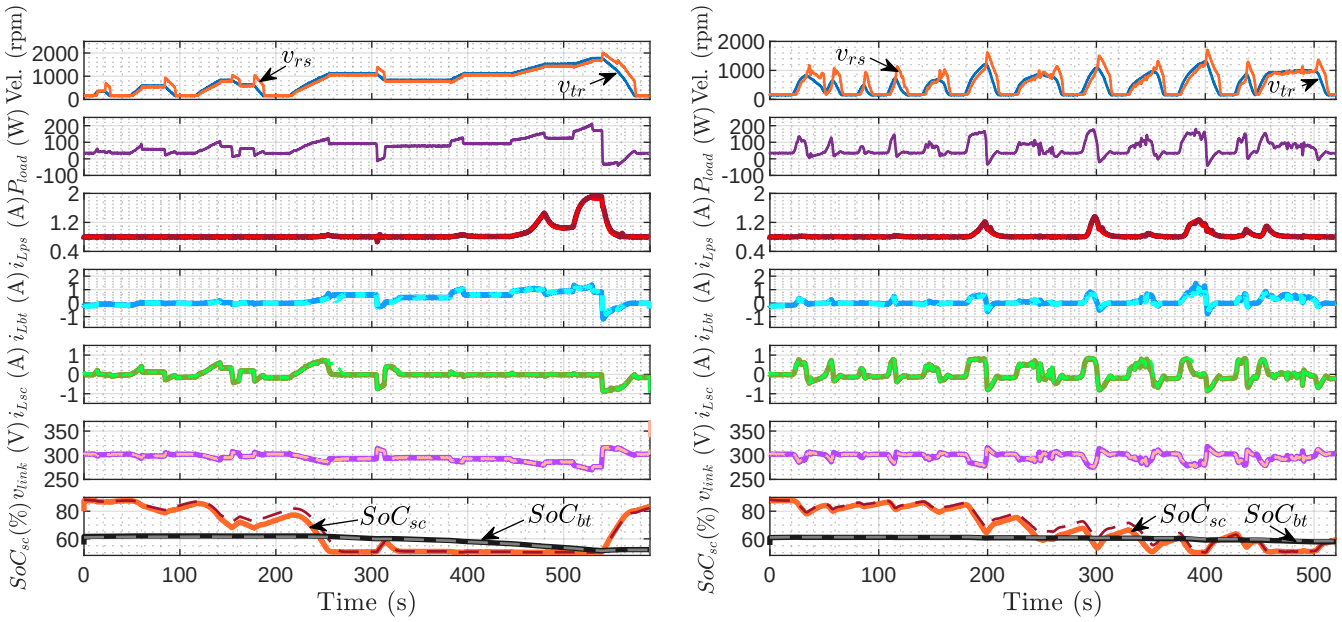

Fig. 12: TIMs velocity signals, SHV low-scale prototype load, and variables dynamics performance on the EMS during (a) NEDC and (b) OCT driving cycle: experimental results (continuous line) versus computational simulation (dashed line).

TABLE IV: Quantitative comparison results of S-shaped and PMP optimal approach.

Cycles		EMS method	Fuel cons. (g)		SoC_{bt} relative error (%)	
NEDC	OCT	PMP	53.83	43.48	4.1	1.64
		S-shaped	52.44	44.06	4.8	1.54

which may be performed in urban, highways, or mountainous roads.

VII. Conclusion

This paper presented an EMS for a SHV under a fully active topology, which was based on S-shaped functions to perform a power sharing between ICE-generator set and HESS. The fully active topology adds to EMS flexibility to manage the sources, with a focus on maximizing the energy usage of the supercapacitors for reducing fuel consumption and battery stress. Additionally, the S-shaped functions were designed to regulate the power of the primary source while maintain the batteries SoC at safe levels. This adaptability was combined with a offline meta-heuristic optimization strategy to tune the control parameters and achieve better performance across different driving cycles. As a result, the developed strategy demonstrated performance comparable to the optimal approach made by the PMP. Regarding the average fuel savings during different driving cycles, the proposed strategy consumption were 8.75% and 28.99% lower compared to HWT+FLC and FLC methods, respectively. Simultaneously, the proposed EMS demonstrated higher energy conversion efficiency compared to other strategies, even when considering all the additional losses from the dc/dc converters.

The stability and performance analysis was conducted using Lyapunov's indirect method and the infinity norm, respectively. This analysis was made possible by the continuity S functions employed on the closed-loop model, which enabled point-to-point analysis for each vehicle load level and HESS SoCs. The results evaluate the stability of the entire control system for different SHV laboratory-scale load operations, involving the supercapacitor and dc-link in critical operations. Thus, this makes the application of S-shaped functions more reliable for fully active topologies.

When the strategy is applied in practice, the fuel consumption reduction obtained from the simulations was validated, with relative errors of 2.58% and 1.33% compared to the PMP. However, a more pronounced fluctuation in the battery SoC was observed in the NEDC drive cycle, which may weaken the expected performance of the proposed strategy applied in different driving cycles patterns. This outcome is attributed to differences in power required by the prototype under highway driving conditions in the NEDC compared to urban driving conditions in Dallas, which were used for tuning the S-function parameters that manage the primary source and supercapacitor energy distribution. Therefore, future work aims to explore real-time tuning of EMS parameters, developing a new control hierarchy to optimize parameters on the scale of minutes or hours for improving the EMS adaptability across different standard driving cycles.

References

[1] C. M. Martinez, X. Hu, D. Cao, E. Velenis, B. Gao, and M. Wellers, "Energy management in plug-in hybrid electric vehicles: Recent progress and a connected vehicles perspective," *IEEE Transactions on Vehicular Technology*, vol. 66, no. 6, pp. 4534–4549, 2016.

[2] A. Biswas and A. Emadi, "Energy management systems for electrified powertrains: State-of-the-art review and future trends," *IEEE Transactions on Vehicular Technology*, vol. 68, no. 7, pp. 6453–6467, 2019.

[3] G. Du, Y. Zou, X. Zhang, L. Guo, and N. Guo, "Heuristic energy management strategy of hybrid electric vehicle based on deep reinforcement learning with accelerated gradient optimization," *IEEE Transactions on Transportation Electrification*, vol. 7, no. 4, pp. 2194–2208, 2021.

[4] A. K. Podder, O. Chakraborty, S. Islam, N. M. Kumar, and H. H. Alhelou, "Control strategies of different hybrid energy storage systems for electric vehicles applications," *IEEE Access*, vol. 9, pp. 51 865–51 895, 2021.

[5] L. J. R. Silva, M. V. R. Campos, B. M. Zilli, T. A. Fagundes, R. V. A. Neves, R. Q. Machado, and V. A. Oliveira, "A sigmoid-weighted-consensus for balancing multiple battery energy storage systems," *IEEE Transactions on Industrial Electronics*, DOI 10.1109/TIE.2024.3443958, pp. 1–11, 2024.

[6] S. J. Ankar and P. K.P., "Optimal sizing and energy management of electric vehicle hybrid energy storage systems with multi-objective optimization criterion," *IEEE Transactions on Vehicular Technology*, vol. 73, DOI 10.1109/TVT.2024.3372137, no. 8, pp. 11 082–11 096, 2024.

[7] M. S. Munsi and H. Chaoui, "Energy management systems for electric vehicles: A comprehensive review of technologies and trends," *IEEE Access*, vol. 12, DOI 10.1109/ACCESS.2024.3371483, pp. 60 385–60 403, 2024.

[8] Y. Xiang and X. Yang, "An ecms for multi-objective energy management strategy of parallel diesel electric hybrid ship based on ant colony optimization algorithm," *Energies*, vol. 14, no. 4, p. 810, 2021.

[9] C. Yang, X. Du, W. Wang, L. Yang, and M. Zha, "A rolling convergent equivalent consumption minimization strategy for plug-in hybrid electric vehicles," *IEEE Transactions on Vehicular Technology*, 2023.

[10] X. Sun, J. Fu, H. Yang, M. Xie, and J. Liu, "An energy management strategy for plug-in hybrid electric vehicles based on deep learning and improved model predictive control," *Energy*, vol. 269, p. 126772, 2023.

[11] J. Gan, S. Li, C. Wei, L. Deng, and X. Tang, "Intelligent learning algorithm and intelligent transportation-based energy management strategies for hybrid electric vehicles: A review," *IEEE Transactions on Intelligent Transportation Systems*, vol. 24, DOI 10.1109/TITS.2023.3283010, no. 10, pp. 10 345–10 361, 2023.

[12] N. Yang, L. Han, R. Liu, Z. Wei, H. Liu, and C. Xiang, "Multiobjective intelligent energy management for hybrid electric vehicles based on multiagent reinforcement learning," *IEEE Transactions on Transportation Electrification*, vol. 9, DOI 10.1109/TTE.2023.3236324, no. 3, pp. 4294–4305, 2023.

[13] X. Tang, J. Chen, K. Yang, M. Toyoda, T. Liu, and X. Hu, "Visual detection and deep reinforcement learning-based car following and energy management for hybrid electric vehicles," *IEEE Transactions on Transportation Electrification*, vol. 8, no. 2, pp. 2501–2515, 2022.

[14] H. Lee and S. W. Cha, "Reinforcement learning based on equivalent consumption minimization strategy for optimal control of hybrid electric vehicles," *IEEE Access*, vol. 9, DOI 10.1109/ACCESS.2020.3047497, pp. 860–871, 2021.

[15] L. Guo, X. Zhang, Y. Zou, N. Guo, J. Li, and G. Du, "Cost-optimal energy management strategy for plug-in hybrid electric vehicles with variable horizon speed prediction and adaptive state-of-charge reference," *Energy*, vol. 232, p. 120993, 2021.

[16] A. S. Mohammed, S. M. Atnaw, A. O. Salau, and J. N. Eneh, "Review of optimal sizing and power management strategies for fuel cell/battery/super capacitor hybrid electric vehicles," *Energy Reports*, vol. 9, pp. 2213–2228, 2023.

[17] K. Yang, X. Tang, S. Qiu, S. Jin, Z. Wei, and H. Wang, "Towards robust decision-making for autonomous driving on highway," *IEEE Transactions on Vehicular Technology*, vol. 72, DOI 10.1109/TVT.2023.3268500, no. 9, pp. 11 251–11 263, 2023.

[18] Y. Chen, S. Li, X. Tang, K. Yang, D. Cao, and X. Lin, "Interaction-aware decision-making for autonomous vehicles," *IEEE Transactions on Transportation Electrification*, vol. 9, no. 3, pp. 4704–4715, 2023.

[19] B. Chen, X. Pan, and S. A. Evangelou, "Optimal energy management of series hybrid electric vehicles with engine start–stop system," *IEEE Transactions on Control Systems Technology*, vol. 31, no. 2, pp. 660–675, 2022.

[20] H.-A. Trinh, H.-V.-A. Truong, and K. K. Ahn, "Development of fuzzy-adaptive control based energy management strategy for pem fuel cell hybrid tramway system," *Applied Sciences*, vol. 12, no. 8, p. 3880, 2022.

[21] F. Tao, L. Zhu, Z. Fu, P. Si, and L. Sun, "Frequency decoupling-based energy management strategy for fuel cell/battery/ultracapacitor hybrid vehicle using fuzzy control method," *IEEE Access*, vol. 8, pp. 166 491–166 502, 2020.

[22] S. Ahmadi, S. Bathaee, and A. H. Hosseinpour, "Improving fuel economy and performance of a fuel-cell hybrid electric vehicle (fuel-cell, battery, and ultra-capacitor) using optimized energy management strategy," *Energy Conversion and Management*, vol. 160, pp. 74–84, 2018.

[23] H. Maghfiroh, O. Wahyunggoro, and A. I. Cahyadi, "Energy management in hybrid electric and hybrid energy storage system vehicles: A fuzzy logic controller review," *IEEE Access*, 2024.

[24] J. Chen, C. Xu, C. Wu, and W. Xu, "Adaptive fuzzy logic control of fuel-cell-battery hybrid systems for electric vehicles," *IEEE Transactions on Industrial Informatics*, vol. 14, no. 1, pp. 292–300, 2016.

[25] J. E. Valdez-Resendiz, J. C. Rosas-Caro, J. C. Mayo-Maldonado, A. Claudio-Sanchez, O. Ruiz-Martinez, and V. M. Sanchez, "Improvement of ultracapacitors-energy usage in fuel cell based hybrid electric vehicle," *International Journal of Hydrogen Energy*, vol. 45, no. 26, pp. 13 746–13 756, 2020.

[26] Z. Fu, L. Zhu, F. Tao, P. Si, and L. Sun, "Optimization based energy management strategy for fuel cell/battery/ultracapacitor hybrid vehicle considering fuel economy and fuel cell lifespan," *International Journal of Hydrogen Energy*, vol. 45, no. 15, pp. 8875–8886, 2020.

[27] M. A. Kamoona, O. C. Kivanc, and O. A. Ahmed, "Intelligent energy management system evaluation of hybrid electric vehicle based on recurrent wavelet neural network and PSO algorithm." *International Journal of Intelligent Engineering & Systems*, vol. 16, no. 1, 2023.

[28] T. A. Fagundes, G. H. F. Fuzato, R. F. Q. Magossi, M. V. R. Campos, B. M. Zilli, A. M. d. S. Alonso, and R. Q. Machado, "Secondary voltage control for dc microgrids: A design perspective for soc with voltage restoration provision," *IEEE Transactions on Smart Grid*, DOI 10.1109/TSG.2024.3433410, pp. 1–1, 2024.

[29] J. Han, A. Khalatbarisoltani, Y. Yang, and X. Hu, "Energy management in plug-in hybrid electric vehicles: Preheating the battery packs in low-temperature driving scenarios," *IEEE Transactions on Intelligent Transportation Systems*, vol. 25, DOI 10.1109/TITS.2023.3317637, no. 2, pp. 1978–1991, 2024.

[30] K. Itani, A. De Bernardinis, Z. Khatir, A. Jammal, and M. Oueidat, "Regenerative braking modeling, control, and simulation of a hybrid energy storage system for an electric vehicle in extreme conditions," *IEEE Transactions on Transportation Electrification*, vol. 2, no. 4, pp. 465–479, 2016.

[31] X. Tang, J. Zhang, X. Cui, X. Lin, L. M. Grzesiak, and X. Hu, "Multi-objective design optimization of a novel dual-mode power-split hybrid powertrain," *IEEE Transactions on Vehicular Technology*, vol. 71, DOI 10.1109/TVT.2021.3130580, no. 1, pp. 282–296, 2022.

[32] M. Kargar, C. Zhang, and X. Song, "Integrated optimization of power management and vehicle motion control for autonomous hybrid electric vehicles," *IEEE Transactions on Vehicular Technology*, vol. 72, DOI 10.1109/TVT.2023.3270127, no. 9, pp. 11 147–11 155, 2023.

[33] H.-B. Yuan, W.-J. Zou, S. Jung, and Y.-B. Kim, "A real-time rule-based energy management strategy with multi-objective optimization for a fuel cell hybrid electric vehicle," *IEEE Access*, vol. 10, DOI 10.1109/ACCESS.2022.3208365, pp. 102 618–102 628, 2022.

[34] M. J. Reddy and D. N. Kumar, "Multiobjective differential evolution with application to reservoir system optimization," *Journal of computing in civil engineering*, vol. 21, no. 2, pp. 136–146, 2007.

[35] M. Leon and N. Xiong, "Investigation of mutation strategies in differential evolution for solving global optimization problems," in *Artificial Intelligence and Soft Computing: 13th International Conference, ICAISC 2014, Zakopane, Poland, June 1-5, 2014, Proceedings, Part I 13*, pp. 372–383. Springer, 2014.

[36] Y. Liu and J. Zhang, "A repeated commuting driving cycle dataset with application to short-term vehicle velocity forecasting," *Journal of Autonomous Vehicles and Systems*, vol. 1, no. 3, p. 031002, 2021.

[37] National Renewable Energy Laboratory, "NREL DriveCAT: Drive Cycle Analysis Tool." www.nrel.gov/transportation/drive-cycle-tool, 2024, online; accessed 10 May 2024.

[38] H. Jiang, L. Xu, J. Li, Z. Hu, and M. Ouyang, "Energy management and component sizing for a fuel cell/battery/supercapacitor hybrid powertrain based on two-dimensional optimization algorithms," *Energy*, vol. 177, pp. 386–396, 2019.

Márcio Von Rondow Campos was born in Caratinga, Brazil. He received the B.S in electrical engineering in 2022 from the Federal University of Viçosa and the M.S. degree in 2024 from the University of Sao Paulo. He is currently working on his Ph.D. in electrical engineering at the University of Sao Paulo and his mains research interest are in the fields of dc/dc converters for renewable energy sources, microgrids, energy management and hybrid electric vehicles.

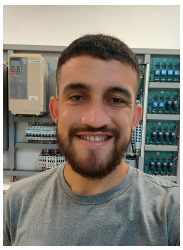

Lucas Jonys Ribeiro Silva was born in Viçosa, Brazil, in 1997. He received the B.S. in electrical engineering in 2020 from The Federal University of Viçosa and the M.S. degree in 2022 from the University of Sao Paulo. He is currently working on his Ph.D. in electrical engineering at the University of Sao Paulo. His main research interest are in the fields of microgrids, electric and hybrid vehicles, energy management and dc/dc converters for renewable energy sources and storage systems.

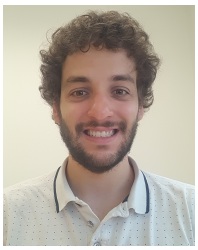

Thales Augusto Fagundes was born in Jundiai, Brazil. He received the B.S. in electrical engineering in 2017 and the M.S. degree in power electronics and dynamic systems in 2020 from the University of Sao Paulo, Sao Carlos, Brazil, where he is currently working on his Ph.D. in microgrids. In 2014, he studied abroad at the University of New South Wales, Sydney, NSW, Australia, focusing on courses related to alternative energy sources. From 2022 to 2023, he was a Visiting Researcher with Aalborg University, Aalborg, Denmark. His research interests include the fields of microgrids, energy management and dc-dc converters for renewable energy sources and storage systems.

Rodolpho Vilela Alves Neves was born in Ipatinga, Brazil. He received the B. S. from the Federal University of Viçosa (UFV), Brazil, in 2011, and the M.Sc. and D.Sc. in Electrical Engineering from the University of Sao Paulo, Sao Carlos, Brazil, in 2013 and 2018, respectively. From 2015 to 2016, he was a Visiting Researcher at Aalborg University, Denmark. He is currently an Adjunct Professor in the Department of Electrical Engineering at UFV. His research interests include intelligent control strategies and modelling dynamic systems.

Vilma Alves de Oliveira (Life Senior Member, IEEE) received the B.Eng. degree in electronics from the Rio de Janeiro State University, Rio de Janeiro, Brazil, in 1976, the M.Sc. degree from the Federal University of Rio de Janeiro, Rio de Janeiro, in 1980, and the Ph.D. degree from the University of Southampton, Southampton, U.K., in 1989, both in electrical engineering. In 1990, she joined the Department of Electrical and Computing Engineering, University of Sao Paulo, Sao Paulo, Brazil, where she is currently a Full Professor. Her research interests include fuzzy control and control design and its applications. Prof. Oliveira is currently the Editor in Chief for the Journal of Control, Automation and Electrical Systems.

Ricardo Quadros Machado (M'2005, SM'2018) was born in Santa Maria, Brazil. He received the B. S. from the University of Santa Maria (Santa Maria, Brazil) in 1997, the M.S. (2000) and the Ph.D. (2005) degrees in Electrical Engineering from the University of Campinas (Campinas, Brazil). From 2002 to 2003 he was a visiting researcher at the University of Padova (Padova, Italy) and from 2005 to 2007 he was a post-doctorate at the Federal University of Santa Maria, (Santa Maria, Brazil). From 2013 to 2014 he was visiting professor at the University of Toronto (Toronto, Canada). Additionally, from 2007 to 2018 he was assistant professor at the University of Sao Paulo (Sao Carlos, Brazil). Currently, he is associated professor at the University of Sao Paulo (Sao Carlos, Brazil) and his main research interests are: processing of energy in dc/dc and dc/ac converters, digital control of power converters, distributed generation systems, smart grids and control of renewable energy sources.